The Astrophysical Journal, 949:110 (11pp), 2023 June 1 https://doi.org/10.3847/1538-4357/acc581

Temporal and Spectral Evolution of Gamma-Ray Burst Broad Pulses: Identification of High-latitude Emission in the Prompt Emission

Donggeun Tak[1,2,3], Z. Lucas Uhm[3], Judith Racusin[4], Bing Zhang[5,6], Sylvain Guiriec[4,7], Daniel Kocevski[8], Bin-Bin Zhang[9], and Julie McEnery[4,10]

[1] Deutsches Elektronen-Synchrotron DESY, Platanenallee 6, D-15738 Zeuthen, Germany; donggeun.tak@gmail.com
[2] SNU Astronomy Research Center, Seoul National University, 1 Gwanak-rho, Gwanak-gu, Seoul, Republic of Korea
[3] Korea Astronomy and Space Science Institute, Daejeon 34055, Republic of Korea
[4] NASA Goddard Space Flight Center, Greenbelt, MD 20771, USA
[5] Nevada Center for Astrophysics, University of Nevada, Las Vegas, NV 89154, USA
[6] Department of Physics and Astronomy, University of Nevada, Las Vegas, NV 89154, USA
[7] Department of Physics, The George Washington University, 725 21st Street NW, Washington, DC 20052, USA
[8] NASA Marshall Space Flight Center, Huntsville, AL 35812, USA
[9] School of Astronomy and Space Science, Nanjing University, Nanjing 210093, People's Republic of China
[10] Department of Physics and Department of Astronomy, University of Maryland, College Park, MD 20742, USA
Received 2022 December 14; revised 2023 March 10; accepted 2023 March 10; published 2023 June 2

Abstract

We perform a detailed analysis of broad pulses in bright gamma-ray bursts (GRBs) to understand the evolution of GRB broad pulses. Using the temporal and spectral properties, we test the high-latitude emission (HLE) scenario in the decaying phase of broad pulses. The HLE originates from the curvature effect of a relativistic spherical jet, where higher-latitude photons are delayed and softer than the observer's line-of-sight emission. The signature of HLE has not yet been identified undisputedly during the prompt emission of GRBs. The HLE theory predicts a specific relation, $F_{\nu,E_p} \propto E_p^2$, between the peak energy E_p in νF_ν spectra and the spectral flux F_ν measured at E_p, F_{ν,E_p}. We search for evidence of this relation in 2157 GRBs detected by the Gamma-ray Burst Monitor on board the Fermi Gamma-ray Space Telescope from 2008 to 2017. After imposing unbiased selection criteria in order to minimize contamination in a signal by background and overlaps of pulses, we build a sample of 32 broad pulses in 32 GRBs. We perform a time-resolved spectral analysis on each of these 32 broad pulses and find that the evolution of 18 pulses (56%) is clearly consistent with the HLE relation. For the 18 broad pulses, the exponent δ in the relation of $F_{\nu,E_p} \propto E_p^\delta$ is distributed as a Gaussian function with a median and width of 1.99 and 0.34, respectively. This result provides a constraint on the emission radius of GRBs with the HLE signature.

Unified Astronomy Thesaurus concepts: Gamma-ray bursts (629); Relativistic jets (1390)

Supporting material: figure set, machine-readable table

1. Introduction

Gamma-ray bursts (GRBs) are the brightest electromagnetic radiation, consisting of a short gamma-ray flash (prompt emission) followed by long-lived, broad energy band radiation (afterglow). They are attributed to emission from an outgoing relativistic jet (for a recent review, see Kumar & Zhang 2015). Since the relativistic jet expands within a few degrees (Sari et al. 1999), the geometry of the outgoing shell plays an important role in forming the observed temporal and spectral shapes (see Figure 1). Due to the Doppler effect, emission from higher latitudes, the so-called "high-latitude emission" (HLE), is observed at a later time with a softer spectrum relative to the line-of-sight emission (LoSE); i.e., the higher the latitude, the smaller the Doppler factor.

The relativistic curvature effect is believed to leave its signature in the temporal and spectral shapes of GRBs in both the prompt emission and afterglow phases (Fenimore et al. 1996; Kumar & Panaitescu 2000; Dermer 2004). Through the use of numerous observations of GRB afterglows, a canonical X-ray afterglow picture has emerged (Nousek et al. 2006; Zhang et al. 2006). Among the distinct afterglow phases commonly observed in the X-ray band, an early steep-decay phase connected with the tail of the prompt emission and a steep-decay phase in an X-ray flare have been interpreted as a result of the HLE effect (e.g., Liang et al. 2006; Yamazaki et al. 2006; Zhang et al. 2006). During these decaying phases, the HLE theory predicts a simple relation between the temporal index $\hat{\alpha}$ and the spectral index $\hat{\beta}$, $\hat{\alpha} = 2 + \hat{\beta}$, in the convention of $F_{\nu\,\mathrm{obs}} \propto t_{\mathrm{obs}}^{-\hat{\alpha}}\, \nu_{\mathrm{obs}}^{-\hat{\beta}}$ (Kumar & Panaitescu 2000). Note that this relation has been successfully satisfied once the onset time of emission is properly estimated (Liang et al. 2006; Zhang et al. 2007, 2009; Jia et al. 2016; Uhm & Zhang 2016a). Also, it is suggested that an X-ray plateau emission can be HLE originated from the structured jet (Ascenzi et al. 2020; Oganesyan 2020). Furthermore, the HLE evidence was also observed in the high-energy (>100 MeV) emission in GRB 131108A (Ajello et al. 2019).

Although such vigorous studies of HLE have been conducted, clear HLE evidence has not been found in the prompt emission of GRBs. Observed spectral lags, the relative time difference of low-energy photons with respect to high-energy photons, have been considered as one of the HLE signatures (e.g., Dermer 2004; Shen et al. 2005). However, Uhm & Zhang (2016b) showed that the spectral lag is not produced by the curvature effect but rather by the combination

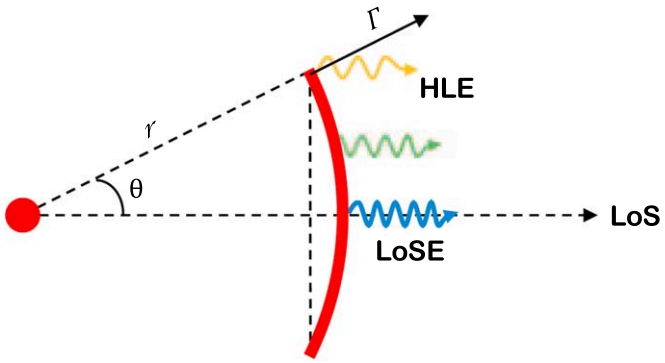

Figure 1. Schematic drawing of the geometry of an outgoing shell. If the shell expands with a Lorentz factor Γ, the photons from the LoS are boosted by 2Γ, while the photons from high latitudes are boosted by $[\Gamma(1-\beta\cos\theta)]^{-1}$ and delayed by $\Delta t = (r/c)(1-\cos\theta)$.

of several physical conditions, such as a large emission radius, a magnetic field decreasing with radius, and bulk acceleration. Ryde & Svensson (2002) and Kocevski et al. (2003) suggested that the asymmetric pulse shape (a fast rise and exponential decay pulse, FRED) commonly observed in the prompt phase can be interpreted as the curvature effect. They derived an analytical function for the asymmetric pulse shape and successfully fit the Burst And Transient Source Experiment (BATSE) data with the asymmetric function. Kocevski et al. (2003) asserted that about 40% of the BATSE sample is consistent with the predicted HLE temporal shape, although most of the others decay faster than predicted. However, as stated by the authors, this method is decoupled from the spectral property of the emission so that it cannot be irrefutable evidence.

There are several difficulties in finding the HLE signature in the prompt emission, especially in the energy spectrum. First of all, the observed temporal and spectral shapes vary one to another. Also, overlaps of multiple pulses (e.g., Norris et al. 1996; Hakkila & Preece 2011) and multiple spectral components in the GRB energy spectrum (e.g., Abdo et al. 2009; Ackermann et al. 2010, 2011; Guiriec et al. 2011, 2015; Zhang et al. 2011; Tak et al. 2019) conceal the temporal and spectral properties of each pulse and the HLE signature. Genet & Granot (2009) modeled the prompt emission considering the HLE effect and cautioned that the HLE relation ($\hat{\alpha} = 2 + \hat{\beta}$) commonly used in the afterglow cannot be tested for a pulse in the prompt emission due to observational effects (e.g., an unclear onset time of each pulse and contamination from overlaps of nearby pulses).

Another predicted HLE relation is a relation between the flux at a specific frequency and that frequency, $F_\nu(\nu_p) \propto \nu_p^2$ (e.g., Dermer 2004; Shenoy et al. 2013; Uhm & Zhang 2015). Indeed, similar relations between the two parameters have been vigorously studied. For example, Borgonovo & Ryde (2001) studied the hardness–intensity correlation, $\nu F_\nu(E_p) \propto E_p^\eta$, with long-duration GRBs (generally $T_{90} > 2$ s)[11] detected by BATSE. Compared to the bolometric flux, the use of the flux at the peak energy, $\nu F_\nu(E_p)$, can alleviate many observational limits, such as limited spectral coverage of detectors and overlap of weak/soft spectral components or pulses. They found that 57% of their sample satisfies the correlation within the prompt emission, and the exponent η is approximately distributed as a normal distribution with a median and width of 2.0 and 0.68, respectively. However, this η value was not consistent with the HLE prediction; the predicted value for the exponent η is 3, $\nu F_\nu(E_p) \propto E_p^3$. Therefore, an unambiguous conclusion has not been drawn in the prompt emission.

Recently, Li & Zhang (2021) tested the curvature effect with the Fermi Gamma-ray Space Telescope (Fermi) GRBs and showed the evidence of bulk acceleration. Uhm et al. (2022) performed a detailed numerical modeling of broad pulses in the prompt emission with a simple physical picture and provided possible scenarios of the HLE signature. In this work, we perform a systematic study of a large sample of broad pulses in the Fermi Gamma-ray Burst Monitor (GBM) GRBs observed from 2008 to 2017 and characterize the temporal and spectral evolutional features. We also test the scaling relation,

$$F_{\nu,E_p} = A E_p{}^{\delta}, \quad (1)$$

in order to identify the HLE signature. First of all, we select bright GRBs and impose several criteria to find relatively clean broad pulses (Section 2). The method for identifying the HLE signature and the result are presented in Sections 3 and 4, respectively. In Section 5, we discuss several implications of the results. Finally, we conclude in Section 6.

2. Sample Selection

Our initial sample consists of 2157 GRBs listed in the Fermi-GBM catalog observed in 2008–2017 (Gruber et al. 2014; von Kienlin et al. 2014; Narayana Bhat et al. 2016; Yu et al. 2016). In order to study the temporal and spectral features of GRB broad pulses, we perform a time-resolved analysis of a sufficient number of bins. Since only bright GRBs can provide well-constrained parameters in the time-resolved spectral analysis, we select GRBs based on energy fluence and peak flux in the energy band from 10 keV to 1 MeV, i.e., the energy fluence and peak flux thresholds are 2.5×10^{-5} erg cm^{-2} and 1.8×10^{-6} erg cm^{-2} s^{-1}, respectively. In this selection process, we adopt the energy fluence and peak flux from the Fermi-GBM online catalog,[12] and 175 GRBs (∼8.1%) survive after applying these threshold cuts.

The Fermi-GBM is composed of 12 NaI detectors (sodium iodide; 8 keV–1 MeV) and two BGO detectors (bismuth germanate; 200 keV–40 MeV). Among 14 GBM TTE data,[13] we configure a data set adopting the set of detectors listed in the "Scat Detector Mask"[14] in the GBM online catalog. For the data set, we gather events of 50–300 keV and apply the Bayesian block algorithm, where photon-counting data are segmented based on a sudden change in count rate (Scargle et al. 2013). We estimate a background rate for each energy channel by extrapolating the polynomial function given by fitting time intervals before and after the burst. Finally, we construct a background-subtracted count-rate curve with the Bayesian block bins.

We define a pulse as a series of bins where the count rates are 3σ above the background level. Among one or more pulses in a GRB, we focus on the brightest pulse with the highest count-rate bin, i.e., for each GRB, we select a single broad

[11] Here T_{90} is a time interval containing 90% of the background-subtracted events from a GRB.

[12] https://heasarc.gsfc.nasa.gov/W3Browse/fermi/fermigbrst.html

[13] Event data with a time precise to 2 μs in 128 energy channels.

[14] A list of GBM detectors that is used in the GBM spectral catalog fits.

pulse target. To define a bright, broad pulse and avoid a selection bias, we impose four criteria to systematically filter out pulses that have noticeable contaminations from background and/or overlapping pulses. Again, to minimize a possible systematic bias, these criteria are not based on any physical models or analytical pulse profiles. For each criterion, we also prescribe a yellow (warning) or red (rule out) flag, depending on the satisfaction level to the criterion.

1. The target pulse (the brightest broad pulse among the pulses in the prompt emission) should contain 90% of the GRB fluence:
   (a) yellow flag, $70\% \leqslant S_p < 90\%$;
   (b) red flag, $S_p < 70\%$,

where S_p is the fluence of the brightest pulse in a GRB. This criterion is directly related to the primary fluence and peak flux threshold cuts. This criterion checks whether the pulse is bright enough for the time-resolved analysis. With this criterion, low-luminous GRBs composed of multiple low-fluence pulses are removed.

2. The decaying phase duration (t_d) in the target pulse should be longer than the rising phase duration (t_r):
   (a) yellow flag, $\frac{t_r}{2} \leqslant t_d < t_r$;
   (b) red flag, $t_d < \frac{t_r}{2}$,

where t_r is defined as the duration from the start of the first bin of a target pulse to the peak of the target pulse, and t_d is defined as the duration from the end of t_r to the end of the last bin of the target pulse.

There is no consensus in the GRB pulse shape, but a single GRB pulse is believed to be asymmetric (FRED; Norris et al. 1996; Ryde & Svensson 2002; Kocevski et al. 2003). A pulse with $t_d \ll t_r$ is likely to be a broad pulse superposed with many FRED pulses, and this criterion is intended to exclude such pulses.

3. The decay phase of the target pulse should be clean, i.e., the count rate of the bins should decrease in time without significant fluctuation. If not, the duration of bumps (t_b) should be short:
   (a) yellow flag, $t_b < \frac{t_d}{4}$;
   (b) red flag, $t_b \geqslant \frac{t_d}{4}$, or $N_b \geqslant 2$,

where N_b is the number of bumps. A bump is defined as a series of irregular bins whose count rates are higher than the previous regular bin. This bump ends when a following count rate becomes lower than the bin before the start of the bump. This criterion is to minimize ambiguity due to the interplay between coexistent pulses. Any subdominant pulses on top of the broad pulse make it difficult to extract the temporal and spectral features of the broad pulse.

4. The target pulse should not overlap with any nearby pulses:
   (a) yellow flag, $t_{\rm sp} \leqslant 10$ s;
   (b) red flag, $t_{\rm sp} \leqslant 5$ s,

where $t_{\rm sp}$ is the separation time between the target pulse and nearby pulses. To check this criterion, we check the count rates of three nearby bins within 5 and 10 s before and after the target pulse. If any nearby pulse has a count rate 3σ above the background level, we prescribe a yellow or red flag depending on the proximity of the pulse overlapping the target pulse.

If the target pulse receives at least one red flag or two yellow flags, the pulse and corresponding GRB are removed from our sample. The results of applying these four criteria to 175 GRBs are presented in Appendix A. After the selection procedure, our final sample consists of 32 bright broad pulses from 32 GRBs.

3. Time-resolved Spectral Analysis

For each broad pulse, we perform a time-resolved spectral analysis with GBM data (TTE) from the selected detectors that were employed for the sample selection (Section 2). For each detector, low- and high-energy regimes are ignored due to overflows of channels; i.e., we use 8 keV–1 MeV for NaIs and 200 keV–40 MeV for BGOs. First of all, we estimate a background rate for each of the GBM detectors with *rmfit* (version 43pr2)[15] by fitting a polynomial function for pre- and post-burst time intervals. We generate the data set by writing out the source and background regions using the selected data and background fit obtained in *rmfit*. Next, we perform the spectral analysis with *Xspec* (version 12.10.0).[16] The decaying phase of a broad pulse is divided into equally spaced bins in the logarithmic space (Table 1). We test three representative models for each time interval: a simple power law (PL), a power law with exponential cutoff (CPL), and the Band function (Band; Band et al. 1993). The discussion on the multiple spectral component model is in Section 5.4. The Poisson data with Gaussian background STATistics (PGSTATs) are adopted to estimate the parameters and their errors. The best-fit model for each time interval is determined by comparing the PGSTATs of each model, similar to the criteria employed by the GBM catalog (Gruber et al. 2014; von Kienlin et al. 2014; Narayana Bhat et al. 2016; Yu et al. 2016); the best-fit model is Band when ΔPGSTAT (CPL − Band) > 11.83 units, CPL when ΔPGSTAT (PL − CPL) > 8.58 units, and PL otherwise.

The value and error of F_{ν,E_p} in CPL or Band cannot be directly computed from the parameter estimation procedure, so we compute them with the Monte Carlo simulation. We synthesize 10^5 spectra with the parameters and corresponding covariance matrix of the best-fit model and compute F_{ν,E_p} for each synthesized spectrum. From the obtained F_{ν,E_p} values, we obtain mean and asymmetric errors of F_{ν,E_p}. Note that we aim to test the scaling relation between E_p and F_{ν,E_p}, so we ignore time intervals where the best-fit model is PL.

Next, we perform the maximum-likelihood analysis to test the scaling relation between E_p and F_{ν,E_p} (Equation (1); bottom left panel of Figure 2). We fit the function to all possible sets of temporally connected points, which should have at least four connected points. We use at least four points because two or three points can be aligned in a specific slope by chance, but the plausibility of four points lining up at the specific value is relatively unlikely.

To identify the HLE signature, we first fix the exponent to be consistent with the HLE prediction, $\delta = 2$. For a set that is well consistent with the HLE relation ($\chi^2_\nu < 2$), we fit the same function again but leave δ free to obtain the true exponent. When any sets of points show δ consistent with the HLE relation within the $\pm 1\sigma$ level, we classify the bright, broad pulse as a "clear" case, except for cases with a large error ($\sigma_\delta > 1.5$). When there are multiple sets of points satisfying the

[15] See https://fermi.gsfc.nasa.gov/ssc/data/analysis/rmfit/ for details.
[16] See https://heasarc.gsfc.nasa.gov/xanadu/xspec/ for details.

Table 1
Spectral Analysis Parameters for Selected GRBs

GRB Name	Pulse Start (s)	Analysis Start (s)	Analysis End (s)	No. of Bins	HLE Evidence	PL Index	χ^2_ν
GRB 081009A	−0.194	1.630	7.130	19	N/A	⋯	⋯
GRB 081221A	16.922	18.290	35.290	19	Clear	1.8 ± 0.6	0.2
GRB 081224A	−0.260	0.500	28.000	14	Clear	2.0 ± 0.4	1.2
GRB 090717A	−0.360	3.400	16.400	13	Weak	⋯	⋯
GRB 090719A	−0.136	3.480	14.480	14	Weak	⋯	⋯
GRB 090820A	29.494	32.830	39.830	21	Clear	2.0 ± 0.9	0.1
GRB 100324B	−0.066	1.130	11.630	21	Clear	2.1 ± 0.4	0.4
GRB 101023A	60.842	60.630	95.130	15	Clear	1.8 ± 0.3	0.5
GRB 110301A	−0.086	1.750	10.250	19	Clear	1.9 ± 0.3	0.3
GRB 110721A	−0.132	0.500	22.500	14	Clear	2.0 ± 1.4	0.1
GRB 110920A	−0.076	5.000	185.500	29	Clear	2.1 ± 1.0	0.1
GRB 120204A	19.636	29.080	62.580	19	N/A	⋯	⋯
GRB 120624B	1.950	10.750	37.750	14	Weak	⋯	⋯
GRB 121122A	−0.062	0.170	11.170	14	N/A	⋯	⋯
GRB 130219A	72.754	77.830	112.330	14	N/A	⋯	⋯
GRB 130305A	0.498	1.830	14.830	9	N/A	⋯	⋯
GRB 131028A	2.482	5.250	31.750	17	Weak	⋯	⋯
GRB 131214A	56.154	60.250	81.750	13	Clear	1.7 ± 0.5	1.7
GRB 140206B	5.202	5.830	27.330	22	Clear	2.3 ± 0.9	1.7
GRB 140329A	19.400	22.500	28.500	14	Clear	2.2 ± 0.8	1.7
GRB 141028A	6.118	7.630	39.130	17	Clear	2.4 ± 1.1	0.6
GRB 150213B	−0.062	2.170	5.170	14	Clear	1.9 ± 0.4	1.1
GRB 150306A	−0.562	2.750	12.750	9	Clear	2.0 ± 0.4	0.4
GRB 150403A	−0.818	3.250	29.750	23	N/A	⋯	⋯
GRB 150902A	−0.032	8.500	14.500	19	Weak	⋯	⋯
GRB 151107B	−0.050	7.250	42.750	12	Clear	2.2 ± 0.5	0.2
GRB 160113A	24.334	28.750	51.250	19	Clear	2.1 ± 0.2	1.0
GRB 160509A	−0.626	8.170	36.670	16	Clear	2.1 ± 0.6	0.3
GRB 160530B	−0.536	3.880	15.880	19	Clear	2.1 ± 0.2	1.8
GRB 160910A	−0.078	6.330	31.830	19	Weak	⋯	⋯
GRB 170921B	−0.152	0.440	37.440	19	N/A	⋯	⋯
GRB 171210A	−0.588	1.500	108.000	24	Weak	⋯	⋯

relation, we take δ from the fit using the largest number of points. For a broad pulse that does not have any series of points consistent with the HLE relation, we assign the pulse to either "weak" or "N/A" after visual inspection. If a pulse shows good agreement with the HLE prediction when excluding few outliers or shows a specific slope different from that of the HLE theory ($\delta \neq 2$), we mark it as a "weak" case. Note that one may classify these weak cases into N/A.

The HLE theory predicts not only the E_p–F_{ν,E_p} relation but also two other scaling relations related to observer time ($t_{\rm obs}$) measured from the beginning of a broad pulse,[17]

$$E_p \propto t_{\rm obs}^{-1},$$
$$F_{\nu,E_p} \propto t_{\rm obs}^{-2}. \quad (2)$$

Compared to the E_p–F_{ν,E_p} relation, it is difficult to test these relations due to the observational limitation that we do not know the true onset time of a broad pulse; the beginning of a broad pulse does not have to be the same as the GRB trigger time (the zero time point (t_0) effect; Zhang et al. 2006). To eliminate the t_0 effect, we define and reset the pulse start time ($t_{0,\rm obs}$) where the background-subtracted count rate starts to rise 3σ above the background level (Table 1). Due to this ambiguity, these relations can only be used for double-checking and/or supporting materials identifying the HLE evidence.

[17] These relations are valid only when the bulk Lorentz factor remains constant. For the case of bulk acceleration or deceleration, the exponent of such relations can change (Uhm & Zhang 2015).

4. Results

Figure 2 shows the analysis result of GRB 160113A as an example. The top left panel shows a count-rate curve in three different energy bands; 10–50, 50–300, and 300–1000 keV. From this panel, one can check the existence of the spectral lag and pulse shapes in different energy bands. Also, we plot the temporal evolution of E_p on top of the count-rate curve to see the correlation between E_p and the light curves. In most cases, either a "hard-to-soft" or a "flux-tracking" pattern is observed, which is consistent with other observational studies (Ford et al. 1995; Liang & Kargatis 1996; Norris et al. 1996; Lu et al. 2012, 2018; Yu et al. 2016). A low-energy photon index, α, versus E_p (top middle panel) and F_{ν,E_p} (top right panel) is plotted in order to see the evolution of α versus E_p and F_{ν,E_p}. The test results of three HLE relations are presented in the bottom panels, E_p–F_{ν,E_p} (left), $t_{\rm obs}$–E_p (middle), and $t_{\rm obs}$–F_{ν,E_p} (right). The analysis results and figures for the complete sample of 32 broad pulses from 32 GRBs are in Appendix B.

From the χ^2 goodness-of-fit test ($\chi^2_\nu < 2$ when $\delta = 2$), we find that the consistency with the HLE relation is observed in 18 out of 32 broad pulses (∼56%). The 18 pulses with the clear signature satisfy not only the HLE relation between E_p and F_{ν,E_p}

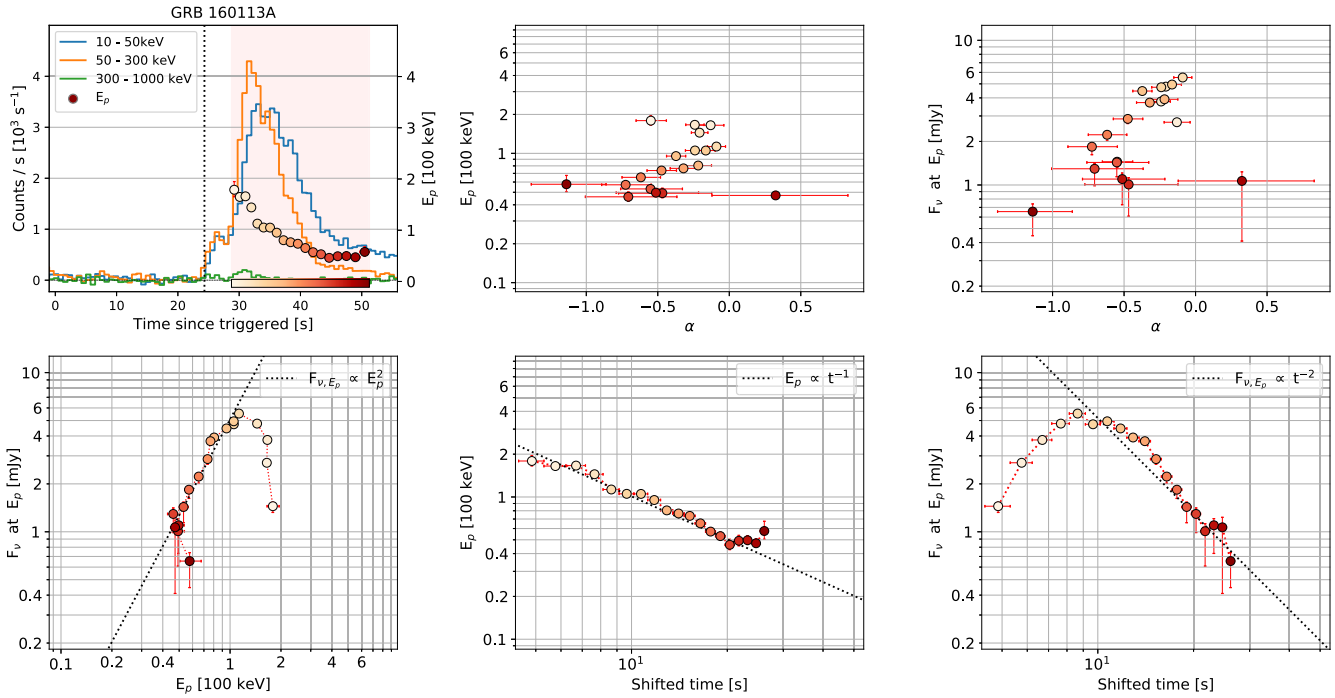

Figure 2. Spectral analysis of a broad pulse in GRB 160113A. The top left panel shows a count-rate curve with the evolution of E_p. The pink shaded region indicates a time interval where either CPL or Band is the best-fit model. The color gradation used in E_p^2 represents the lapse of time, and the color coding is used in the other panels. The other two top panels (middle and right) show α vs. E_p and α vs. F_{ν,E_p}, respectively. The bottom panels show the agreement between the data and the HLE relations: E_p–F_{ν,E_p}, t–E_p, and t–F_{ν,E_p} from left to right. The dotted lines in the bottom panels indicate the lines predicted by the HLE theory.

but also, in most cases, the other HLE relations, $t_{\rm obs}$–E_p and $t_{\rm obs}$–F_{ν,E_p}. Furthermore, as shown in Table 1, the clear cases show $\delta \sim 2$ when we let δ be free. The distribution of δ clearly resembles the normal distribution (Figure 3). We estimate the median and width of the distribution from the Monte Carlo simulation: $\delta = 1.99^{+0.14}_{-0.14}$ and $\sigma_\delta = 0.34^{+0.21}_{-0.13}$, respectively.

5. Discussion

5.1. t *versus* E_p *and* t *versus* F_{ν,E_p}

The GRBs with the clear HLE signature generally satisfy all three HLE predictions. However, in a few cases, we can see a deviation in the scaling relations related to $t_{0,\rm obs}$ (Equation (2)), especially conspicuous in $t_{\rm obs}$–F_{ν,E_p} space; the observed data are aligned but show a slope steeper than the HLE expectation, e.g., GRB 100324B (Figure 5.7), GRB 110301A (Figure 5.9), and GRB 160530B (Figure 5.29).

A simple explanation for these exceptions is usage of an inaccurate value of $t_{0,\rm obs}$. The true onset time, $t_{0,\rm true}$, cannot be exactly measured from observed data due to inevitable observational limits, such as the background fluctuation, detector sensitivity, and/or overlaps of pulses. The combination of these effects hides the true beginning of a broad pulse, resulting in $t_{0,\rm obs}$ later than $t_{0,\rm true}$ ($t_{0,\rm obs} \gtrsim t_{0,\rm true}$). These observational effects can lead to the deviation in the slopes of $t_{\rm obs}$–E_p and $t_{\rm obs}$–F_{ν,E_p}.

Another explanation for the steeper slopes can be the effect arising from the bulk acceleration (Uhm & Zhang 2015, 2016a; Uhm et al. 2018; Li & Zhang 2021).

5.2. Interesting Cases: δ of 0.7

There are two pulses showing a break in their E_p–F_{ν,E_p} curve: GRB 110920A (clear; Figure 5.11) and GRB 171210A (weak; Figure 5.32). For these GRBs, we compute δ for before and after the break.

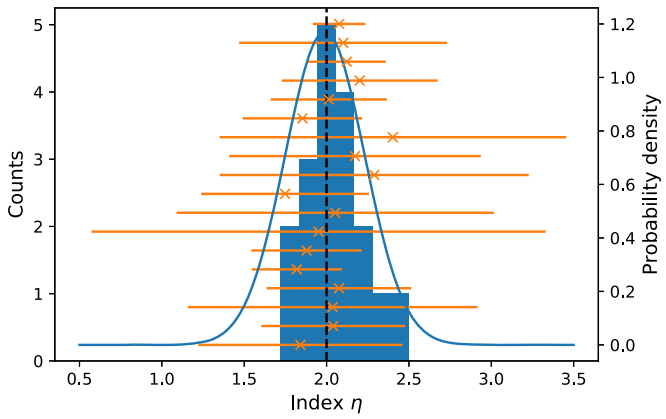

Figure 3. Distribution of δ. The blue bar is the distribution of δ, and the blue line shows a normal probability function given by the Monte Carlo simulation with 18 broad pulses. The median and width of the distribution are 1.99 and 0.34, respectively. The orange error bars indicate the fit results of 18 GRBs clearly exhibiting the HLE signature. The black dotted line represents the HLE expectation, $\delta = 2$, and the data and corresponding distribution agree with the HLE theory.

Object GRB 110920A has $\delta_{110920A,\rm before} = 0.7 \pm 0.1$ and $\delta_{110920A,\rm after} = 2.1 \pm 1.0$. We emphasize that Shenoy et al. (2013) also analyzed GRB 110920A and found that the slope η in $(\nu F_\nu)_{E_p} \propto E_p{}^\eta$ is 1.64 ± 0.01, which is consistent with $\delta_{110920A,\rm before}$ ($\eta \simeq \delta + 1$). This implies that η from Shenoy et al. (2013) is likely to be computed by the data points before the break. In the case of GRB 171210A, the exponents are $\delta_{171210A,\rm before} = 0.7 \pm 0.1$ and $\delta_{171210A,\rm after} = 4.0 \pm 0.3$. Interestingly, before the break, the slopes of two GRBs are consistent, $\delta \sim 0.7$. Also, we found a similar slope in

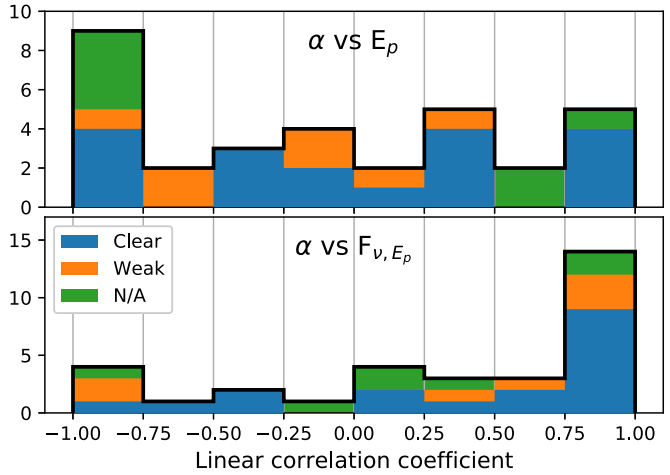

Figure 4. Stacked distributions of the linear correlation coefficients. The top panel is the correlation between α and E_p, and the bottom panel is α and F_{ν,E_p}.

GRB 131028A (weak; Figure 5.17), $\delta_{131028A} = 0.7 \pm 0.1$. Note that GRB 131028A is assigned to "weak" because the slope is not consistent with the HLE prediction.

In these three GRBs, the common slope of $\delta \sim 0.7$ is made up of a large number of data points, so it is evident that this slope is not built up by chance. Also, this slope is observed regardless of the existence of the HLE signature. Therefore, it is plausible that there would be another physical explanation for this slope.

5.3. Evolution of the Low-energy Photon Index α

We find that many GRBs show a linear correlation between parameters, α versus E_p and α versus F_{ν,E_p} (see Figure 2), especially when the consistency with HLE is clear. We compute the linear correlation coefficient between such parameters for the last four time intervals. We use the last four time intervals because the HLE signature is expected to show up in late time intervals. As shown in Figure 4, the correlation between α and F_{ν,E_p} is apparent compared to the correlation between α and E_p. In both the clear and weak samples, there are many cases that show the positive α–F_{ν,E_p} correlation, whereas the N/A sample occasionally shows the positive correlation.

This α–F_{ν,E_p} correlation may be attributed to the curvature effect. Uhm et al. (2022) found that the peak of the νF_ν spectrum is dominated by HLE, and the energy spectrum below E_p is obtained as the combined effect of the two spectra, LoSE and HLE. This implies that α is not solely given by LoSE but is affected by HLE. Therefore, the linearity of α–F_{ν,E_p} can be related to the HLE effect. We note, though, that this conclusion is drawn from a relatively small number of data points and calls for further studies to understand the physical origin of this correlation.

5.4. Effects of Overlapping Components in the Energy Spectrum

In this study, we assume that each time-resolved energy spectrum is dominated by a single spectral component, which can be PL, CPL, or the Band function. We acknowledge that the best fit for each time interval may be a combination of multiple spectral components as observed in many GRBs (e.g., Guiriec et al. 2011, 2015; Tak et al. 2019). However, if one component overwhelms the other components so that a single component model can adequately describe the peak of the energy spectrum, it is still possible to search for the HLE signature by testing a single spectral component. The clearly observed scaling relation supports that the analysis with a single component is valid because it is difficult to explain the specific evolution of E_p and F_{ν,E_p} in the presence of equally bright multiple spectral components. With the multicomponent analysis, we expect to find the HLE signature in a GRB that does not show clear evidence in this study due to the overlaps of equally bright multiple spectral components. However, the multicomponent analysis requires a more sophisticated method to minimize systematic effects, e.g., tracking the evolution of each spectral component out of multiple components.

5.5. Comparison with Other Relations

In many observational studies, a correlation between E_p and other physical parameters has been studied in a time-resolved spectral analysis. Borgonovo & Ryde (2001) performed a time-resolved analysis with GRBs detected by BATSE and found that $(\nu F_\nu)_{,E_p} \propto {E_p}^{2.0\pm0.68}$. This is not consistent with the HLE theory but may be consistent with $\delta \sim 0.7$ (equivalent to $\eta \sim 1.7$). In addition, many authors have searched for an empirical relation between the bolometric flux and E_p (e.g., Golenetskii et al. 1983; Kargatis et al. 1995; Guiriec et al. 2015). Assuming that $(\nu F_\nu)_{,E_p}$ is proportional to the bolometric flux, the slopes of many empirical relations are rather similar to $\delta = 0.7$. The reason for the discrepancy between this study (the HLE relation) and the slopes of many other empirical relations may result from the fact that most of such empirical relations are computed around the peak of a broad pulse (the early phase), whereas our studies focus on the tail of the broad pulse. As shown in many pulses (see Appendix B), the exponent δ tends to be shallower in the early phase (around the peak) compared to the later phase (the tail).

5.6. Scaling Relations from Other Processes

A scaling relation between $F_\nu(\nu_p)$ and ν_p can result from other physical processes. Wang et al. (2000) performed a simulation study of the GRB spectrum considering the cooling of relativistic electrons in an internal shock scenario. They did not provide the scaling relation between $F_\nu(\nu_p)$ and ν_p but showed the temporal evolution of the peak energy in the νF_ν spectra (Figure 5 in Wang et al. 2000). In the figure, the energy flux at ν_p appears to decay significantly slower than that of the HLE expectation. This implies that the electron cooling alone cannot account for the observed scaling relation.

On the other hand, the synchrotron emission from the external forward shock, which is accompanied by bulk deceleration, can produce a scaling relation between F_ν and ν at the synchrotron characteristic frequencies (ν_{ch}). According to the external forward shock model, $F_\nu(\nu_{ch})$ and ν_{ch} can be described as a function of time, providing specific scaling relations (e.g., Sari et al. 1998; Granot & Sari 2002). Depending on the circumburst density profile and the cooling regime, the exponent of the scaling relation is determined. If our observed break corresponds to the highest characteristic frequency among two frequencies related to the cooling or minimum electron Lorentz factors, in the slow cooling regime, the relation is $F_\nu(\nu_{ch}) \propto \nu_{ch}^{(p-1)}$ (uniform medium) or $F_\nu(\nu_{ch}) \propto \nu_{ch}^{(1-2p)}$ (wind medium), where p is the electron

spectral index. In the fast cooling regime, the relation is $F_\nu(\nu_{\rm ch}) \propto \nu_{\rm ch}^{-1/3}$ regardless of the density profile. Those relations are unlikely to produce the observed $F_\nu(\nu_p) \propto \nu_p^2$ relation with a reasonable value of the electron spectral index p.

6. Conclusion

In this work, we selected 32 broad pulses in 32 GRBs from 175 bright GRBs by imposing reasonable selection criteria and performed a time-resolved spectral analysis of those GRBs. We tested the HLE relation, $F_{\nu,E_p} \propto E_p^2$, and found that 18 out of 32 broad pulses exhibit consistency with the relation. The exponent δ in the HLE relation (Equation (1)) is distributed as the normal distribution with a median and width of 1.99 and 0.34, respectively. The clear sample also satisfied the other two HLE relations, $t_{\rm obs}$–E_p and $t_{\rm obs}$–F_{ν,E_p} (Equation (2)), which supports that the identification of the HLE relation is not made accidentally. Our result agrees with the prediction of the HLE theory and successfully identifies the relation during the prompt emission for the first time. The HLE signature is not expected to be observed in all GRBs because the HLE could be buried under LoSE, depending the physical conditions in the emitting region (Uhm et al. 2022).

Other than the HLE signature, we found several unusual features. We found a δ of 0.7 in three GRBs, which can be associated with a different physical origin. In particular, GRB 110920A shows a break in the E_p and F_{ν,E_p} evolution and has two distinct δ values, 0.7 (before the break) and 2 (after the break). The later δ value is consistent with the HLE prediction, whereas the former value might originate from a different physical process. We also found that there may be a positive correlation between α and F_{ν,E_p}, i.e., as F_{ν,E_p} decreases, α softens. Since this correlation is noticeably observed only in GRBs having clear or weak HLE evidence, the correlation may be related to HLE.

The observation of the HLE evidence in relatively long GRBs ($T_{90} \gtrsim 10$ s) implies that the emission radius for those GRBs is $r \sim 10^{16}$ cm (Uhm et al. 2022). This large emission radius of the gamma ray–emitting region disfavors some prompt emission models, such as the photosphere or internal shock model, but favors the magnetic dissipation models that invoke a large dissipation radius, such as the ICMART model (Zhang & Yan 2011).

D.T. acknowledges the Young Investigators Program of the Helmholtz Association. D.T. and Z.L.U. are supported by National Research Foundation of Korea (NRF) grant No. 2021M3F7A1084525, funded by the Korean government (MSIT). B.B.Z. acknowledges support by the National Key Research and Development Programs of China (2018YFA0404204, 2022YFF0711404, 2022SKA0130102), the National Natural Science Foundation of China (grant Nos. 11833003, U2038105, and 12121003), the science research grants from the China Manned Space Project with NO.CMS-CSST-2021-B11, and the Program for Innovative Talents, Entrepreneur in Jiangsu.

Appendix A
Table of Parameters Related to Selection Criteria

Table 2 shows the results of applying the selection criteria for 32 pulses in 32 GRBs.

Table 2
Selection Criteria for 175 GRBs

Trigger Name	Fluence (10^{-5} erg cm^{-2})	Peak Flux (10^{-6} erg cm^{-2} s^{-1})	Flu.%	t_{rise} (s)	t_{decay} (s)	t_{bumps} (s)	Criteria[a]				
							1	2	3	4	Final
bn080723557	8.3	5.5	20	1.7	1.3	0.0	X	△	⋯	X	⋯
bn080723985	3.6	2.4	72	11.7	3.4	0.0	△	X	⋯	⋯	⋯
bn080817161	5.5	3.1	100	7.8	17.1	9.5	⋯	⋯	X	⋯	⋯
bn080825593	3.7	5.0	55	3.2	4.6	1.3	X	⋯	X	X	⋯
bn080916009	8.3	3.7	100	2.7	45.9	20.1	⋯	⋯	X	△	⋯
bn081009140	3.7	8.2	100	3.0	4.3	0.9	⋯	⋯	△	⋯	O
bn081215784	5.4	23.1	100	1.9	6.2	3.6	⋯	⋯	X	⋯	⋯
bn081221681	2.9	2.4	100	4.4	11.3	0.8	⋯	⋯	△	⋯	O
bn081224887	3.6	6.7	100	2.7	10.0	0.0	⋯	⋯	⋯	⋯	O
bn090102122	3.3	3.0	35	0.2	3.3	2.7	X	⋯	X	X	⋯
bn090217206	3.2	3.1	100	6.0	6.8	6.2	⋯	⋯	X	X	⋯
bn090323002	12.5	3.2	62	29.1	5.3	0.4	X	X	△	△	⋯
bn090328401	5.2	4.1	75	14.2	4.3	0.0	△	X	⋯	X	⋯
bn090424592	4.6	10.8	100	4.4	1.5	0.5	⋯	X	X	X	⋯
bn090528516	4.4	1.9	18	2.7	2.4	0.0	X	△	⋯	X	⋯
bn090618353	27.0	13.7	85	14.1	33.3	14.8	△	⋯	X	⋯	⋯
bn090626189	7.2	5.1	18	2.8	1.6	0.0	X	△	⋯	X	⋯
bn090717034	2.7	2.0	70	5.6	7.3	0.0	△	⋯	⋯	⋯	O
bn090719063	4.7	7.0	100	5.2	8.5	0.0	⋯	⋯	⋯	⋯	O
bn090820027	15.2	23.0	100	5.2	10.4	2.3	⋯	⋯	△	⋯	O
bn090829672	9.1	6.5	89	13.0	14.4	3.8	△	⋯	X	⋯	⋯
bn090902462	27.9	19.9	99	15.2	8.4	5.3	⋯	△	X	⋯	⋯
bn090926181	15.3	18.6	100	4.5	13.4	7.9	⋯	⋯	X	⋯	⋯
bn091003191	3.6	8.5	60	2.5	3.4	0.9	X	⋯	X	X	⋯
bn091030828	3.3	3.3	51	1.5	8.2	0.0	X	⋯	⋯	X	⋯
bn100116897	3.7	4.6	94	7.2	5.4	0.0	⋯	△	⋯	X	⋯
bn100322045	6.3	2.2	68	14.0	6.7	0.0	X	X	⋯	X	⋯
bn100324172	4.5	5.3	100	5.0	6.8	0.0	⋯	⋯	⋯	⋯	O
bn100414097	9.2	5.5	100	24.2	1.8	0.0	⋯	X	⋯	⋯	⋯
bn100511035	3.1	3.5	63	2.1	6.3	0.8	X	⋯	X	X	⋯
bn100528075	3.0	2.5	94	8.0	7.5	1.0	⋯	△	△	X	⋯
bn100701490	2.9	8.8	14	0.3	0.3	0.1	X	△	X	X	⋯
bn100719989	5.1	15.2	88	1.4	4.4	1.6	△	⋯	X	⋯	⋯
bn100724029	24.3	6.5	97	61.0	23.8	5.9	⋯	X	X	⋯	⋯
bn100728095	12.0	3.2	72	37.2	11.5	4.4	△	X	X	X	⋯
bn100826957	18.2	8.2	70	21.5	25.7	4.6	X	⋯	X	⋯	⋯
bn100906576	2.6	2.1	100	11.0	2.0	0.0	⋯	X	⋯	⋯	⋯
bn100918863	14.9	3.7	67	46.0	12.9	0.0	X	X	⋯	△	⋯
bn101014175	17.9	12.7	33	1.8	9.3	7.2	X	⋯	X	X	⋯
bn101023951	5.8	5.6	100	4.6	14.4	2.0	⋯	⋯	△	⋯	O
bn101123952	12.0	9.6	81	11.4	9.4	4.0	△	△	X	⋯	⋯
bn110102788	4.1	2.8	65	11.7	3.6	0.0	X	X	⋯	⋯	⋯
bn110123804	2.6	1.9	86	10.5	5.2	0.0	△	X	⋯	X	⋯
bn110301214	3.8	10.7	100	4.0	2.9	0.0	⋯	△	⋯	⋯	O
bn110407998	2.9	4.6	100	3.5	6.6	1.8	⋯	⋯	X	⋯	⋯
bn110622158	5.5	1.9	100	15.5	26.1	7.0	⋯	⋯	X	⋯	⋯
bn110625881	7.0	12.2	61	3.2	6.8	2.4	X	⋯	X	⋯	⋯
bn110709642	4.3	3.6	11	2.2	0.6	0.0	X	X	⋯	X	⋯
bn110717319	4.8	2.3	85	12.9	3.8	2.0	△	X	X	⋯	⋯
bn110721200	3.9	6.0	100	2.4	9.0	0.0	⋯	⋯	⋯	⋯	O
bn110729142	5.6	1.8	100	10.3	4.3	1.3	⋯	X	X	⋯	⋯
bn110825102	4.7	12.0	100	4.4	4.5	2.6	⋯	⋯	X	⋯	⋯
bn110919634	2.7	1.8	100	14.6	10.1	1.6	⋯	△	△	⋯	⋯
bn110920546	15.9	4.3	100	10.9	78.1	0.0	⋯	⋯	⋯	⋯	O
bn110921912	3.7	7.9	83	2.6	5.4	1.5	△	⋯	X	△	⋯
bn111220486	5.7	6.1	65	7.6	7.2	1.4	X	△	△	X	⋯
bn120119170	3.9	3.0	100	11.4	17.7	6.1	⋯	⋯	X	⋯	⋯
bn120129580	5.7	32.2	100	1.6	3.2	0.8	⋯	⋯	X	⋯	⋯
bn120204054	9.5	4.4	95	13.1	32.1	3.7	⋯	⋯	△	⋯	O
bn120226871	6.1	2.0	100	16.8	22.3	16.0	⋯	⋯	X	⋯	⋯
bn120316008	2.5	1.9	23	1.2	0.7	0.0	X	△	⋯	X	⋯
bn120328268	8.3	7.2	100	5.9	28.1	12.7	⋯	⋯	X	⋯	⋯

Table 2
(Continued)

Trigger Name	Fluence (10^{-5} erg cm^{-2})	Peak Flux (10^{-6} erg cm^{-2} s^{-1})	Flu.%	t_{rise} (s)	t_{decay} (s)	t_{bumps} (s)	Criteria[a] 1	2	3	4	Final
bn120526303	13.4	3.2	78	1.8	32.9	31.9	△	⋯	X	X	⋯
bn120624933	19.6	5.2	100	9.6	7.0	0.0	⋯	△	⋯	⋯	O
bn120707800	10.3	7.4	100	27.2	11.0	0.0	⋯	X	⋯	⋯	⋯
bn120711115	19.7	8.0	100	33.1	12.3	4.9	⋯	X	X	⋯	⋯
bn120728434	12.8	4.2	36	2.6	19.8	6.9	X	⋯	X	⋯	⋯
bn121122885	5.3	7.2	100	1.7	7.4	1.3	⋯	⋯	△	⋯	O
bn121225417	7.3	5.1	16	1.9	2.2	1.0	X	⋯	X	X	⋯
bn130121835	4.6	3.9	100	6.3	12.4	0.7	⋯	⋯	△	X	⋯
bn130219775	3.3	3.0	91	7.8	12.4	0.0	⋯	⋯	⋯	⋯	O
bn130304410	4.7	3.3	86	3.3	8.6	7.7	△	⋯	X	X	⋯
bn130305486	6.0	10.1	100	5.9	8.9	0.0	⋯	⋯	⋯	△	O
bn130306991	16.8	4.9	100	11.4	12.7	7.0	⋯	⋯	X	△	⋯
bn130327350	5.3	2.7	28	1.2	6.5	3.2	X	⋯	X	X	⋯
bn130425327	5.2	3.4	27	0.7	1.6	0.4	X	⋯	X	X	⋯
bn130427324	141.2	176.0	93	5.6	60.4	13.7	⋯	⋯	X	⋯	⋯
bn130502327	11.4	11.0	14	2.2	1.0	0.0	X	X	⋯	X	⋯
bn130504978	13.3	10.9	64	22.7	4.5	0.0	X	X	⋯	⋯	⋯
bn130518580	10.0	11.8	100	11.9	11.0	0.9	⋯	△	△	⋯	⋯
bn130606497	20.9	17.2	57	9.2	13.1	3.9	X	⋯	X	X	⋯
bn130609902	6.5	3.5	100	7.7	19.7	6.4	⋯	⋯	X	⋯	⋯
bn130704560	2.5	5.5	100	4.0	2.0	0.3	⋯	△	△	⋯	⋯
bn130715906	4.4	2.5	100	23.1	15.3	2.9	⋯	△	X	⋯	⋯
bn130720582	10.3	2.2	69	35.6	13.9	2.1	X	X	△	△	⋯
bn130821674	7.1	4.9	69	9.5	7.5	1.5	X	△	△	X	⋯
bn131014215	18.7	87.1	100	1.7	4.3	1.8	⋯	⋯	X	⋯	⋯
bn131028076	16.1	28.4	100	5.8	10.9	0.0	⋯	⋯	⋯	⋯	O
bn131108862	3.6	4.5	20	0.3	1.6	1.1	X	⋯	X	X	⋯
bn131118958	8.0	3.2	9	1.3	0.3	0.0	X	X	⋯	X	⋯
bn131122490	3.5	3.4	35	0.7	3.8	1.8	X	⋯	X	X	⋯
bn131127592	4.0	4.1	78	5.5	8.5	1.6	△	⋯	X	X	⋯
bn131214705	6.5	3.0	76	7.4	14.5	0.0	△	⋯	⋯	⋯	O
bn131229277	2.7	7.7	75	3.0	2.1	0.8	△	△	X	X	⋯
bn131231198	15.3	14.8	100	21.4	25.6	6.8	⋯	⋯	X	⋯	⋯
bn140206275	12.8	9.8	97	8.6	29.7	5.4	⋯	⋯	△	⋯	O
bn140306146	7.4	5.9	56	1.9	8.2	7.6	X	⋯	X	X	⋯
bn140323433	3.0	2.1	20	1.7	1.2	0.0	X	△	⋯	X	⋯
bn140329295	7.2	21.5	95	4.7	4.5	0.0	⋯	△	⋯	⋯	O
bn140416060	7.9	8.2	53	7.2	3.5	1.2	X	X	X	X	⋯
bn140508128	6.4	12.3	60	2.7	5.1	0.0	X	⋯	⋯	X	⋯
bn140512814	4.5	2.5	52	6.4	10.3	4.7	X	⋯	X	X	⋯
bn140523129	5.3	7.2	17	1.0	1.6	0.0	X	⋯	⋯	X	⋯
bn140721336	5.1	2.4	56	6.0	2.1	0.0	X	X	⋯	X	⋯
bn140810782	11.8	5.2	29	6.8	3.1	0.0	X	X	⋯	X	⋯
bn140821997	6.4	4.8	100	20.0	13.0	1.9	⋯	△	X	⋯	⋯
bn141022087	9.5	18.1	100	5.7	3.0	1.7	⋯	△	X	X	⋯
bn141028455	4.0	4.3	100	7.2	12.2	0.8	⋯	⋯	△	⋯	O
bn141029134	4.2	4.5	58	3.7	3.9	1.2	X	⋯	X	X	⋯
bn141207800	3.7	4.5	76	6.8	3.1	1.8	△	X	X	X	⋯
bn141215560	2.9	4.7	30	0.6	1.3	0.3	X	⋯	△	X	⋯
bn141222691	2.6	3.1	60	3.9	4.7	0.0	X	⋯	⋯	X	⋯
bn150118409	14.9	13.1	21	2.9	3.3	0.4	X	⋯	X	X	⋯
bn150201574	6.7	9.5	100	1.9	16.0	6.1	⋯	⋯	X	⋯	⋯
bn150202999	3.5	4.4	100	4.8	8.3	4.0	⋯	⋯	X	⋯	⋯
bn150210935	3.0	10.8	92	1.3	2.2	1.0	⋯	⋯	X	X	⋯
bn150213001	3.0	12.7	100	2.3	3.1	0.0	⋯	⋯	⋯	⋯	O
bn150220598	2.8	2.4	47	2.2	1.8	0.0	X	△	⋯	X	⋯
bn150306993	3.0	4.0	100	3.9	9.3	0.0	⋯	⋯	⋯	⋯	O
bn150309958	4.2	2.5	100	16.4	11.3	2.0	⋯	△	△	⋯	⋯
bn150314205	8.9	16.0	100	1.4	11.0	1.5	⋯	⋯	X	⋯	⋯
bn150330828	14.7	10.4	89	6.9	24.6	12.0	△	⋯	X	⋯	⋯
bn150403913	6.4	9.1	100	10.5	13.5	0.0	⋯	⋯	⋯	⋯	O
bn150510139	9.9	12.9	90	0.2	28.3	23.4	△	⋯	X	X	⋯

Table 2
(Continued)

Trigger Name	Fluence (10^{-5} erg cm^{-2})	Peak Flux (10^{-6} erg cm^{-2} s^{-1})	Flu.%	t_{rise} (s)	t_{decay} (s)	t_{bumps} (s)	Criteria[a] 1	2	3	4	Final
bn150523396	3.7	3.6	55	6.2	2.9	0.0	X	X	…	…	…
bn150627183	18.5	10.5	58	27.4	13.9	6.7	X	△	X	…	…
bn150724782	3.6	3.0	88	11.3	3.2	0.8	△	X	X	X	…
bn150821406	7.1	2.1	100	15.2	42.5	12.4	…	…	X	…	…
bn150902733	8.7	13.5	100	9.3	11.7	0.8	…	…	△	…	O
bn151030999	5.5	3.1	89	14.0	15.0	12.0	△	…	X	…	…
bn151107851	2.8	3.7	100	8.6	11.6	0.0	…	…	…	…	O
bn151227218	4.5	7.6	78	7.1	7.9	1.3	△	…	X	X	…
bn151231443	9.4	9.8	53	6.2	9.5	0.6	X	…	△	X	…
bn160106948	5.1	6.1	71	3.3	11.9	5.0	△	…	X	…	…
bn160107931	2.9	2.3	38	0.3	3.8	0.8	X	…	△	X	…
bn160113398	3.5	3.1	100	7.9	9.5	0.0	…	…	…	…	O
bn160118060	3.5	3.2	23	0.6	1.2	0.0	X	…	…	X	…
bn160215773	6.4	4.2	100	17.8	14.2	4.3	…	△	X	…	…
bn160421137	4.3	2.8	100	12.3	4.3	1.1	…	X	X	…	…
bn160422499	9.0	17.8	100	8.4	5.5	0.7	…	△	△	…	…
bn160509374	20.4	14.9	92	14.6	20.1	2.6	…	…	△	…	O
bn160530667	9.8	18.4	100	6.4	9.8	0.4	…	…	△	…	O
bn160625945	66.8	66.6	99	4.4	33.5	18.1	…	…	X	…	…
bn160720767	15.4	11.2	100	11.8	17.1	3.3	…	…	△	X	…
bn160802259	6.3	17.6	81	1.2	5.1	1.7	△	…	X	△	…
bn160816730	3.4	6.1	68	1.1	3.6	2.8	X	…	X	X	…
bn160821857	54.8	33.4	100	25.7	45.2	4.9	…	…	X	…	…
bn160905471	11.2	6.1	92	18.7	5.0	0.3	…	X	△	△	…
bn160910722	8.6	20.1	100	8.4	14.2	0.0	…	…	…	…	O
bn161020759	3.1	4.1	82	3.5	7.2	1.2	△	…	△	X	…
bn161206064	3.9	3.5	92	8.4	9.6	1.8	…	…	X	X	…
bn161218356	8.8	9.4	81	2.2	19.5	17.1	△	…	X	X	…
bn161229878	4.2	3.1	29	2.9	3.4	2.2	X	…	X	X	…
bn170115743	7.5	8.9	29	1.4	1.3	0.5	X	△	X	X	…
bn170121614	3.5	2.4	59	9.7	5.1	0.0	X	△	…	X	…
bn170207906	6.0	7.5	49	2.0	4.2	1.7	X	…	X	X	…
bn170210116	11.5	7.3	100	7.3	29.2	16.5	…	…	X	X	…
bn170214649	19.8	4.4	90	46.7	31.1	24.3	…	△	X	X	…
bn170228794	2.6	3.5	100	1.4	6.4	0.0	…	…	…	X	…
bn170405777	8.1	3.5	78	30.3	26.6	12.5	△	△	X	△	…
bn170409112	31.9	29.1	100	15.7	36.5	18.5	…	…	X	…	…
bn170510217	5.5	3.5	100	16.4	6.2	1.0	…	X	X	…	…
bn170511249	3.3	2.5	85	2.8	12.5	3.9	△	…	X	X	…
bn170527480	9.2	8.1	63	1.2	14.8	13.1	X	…	X	X	…
bn170607946	5.9	3.9	100	19.5	1.6	0.0	…	X	…	…	…
bn170614486	2.7	2.4	100	10.7	1.2	0.0	…	X	…	…	…
bn170808936	11.9	23.7	100	16.9	8.9	1.6	…	△	X	…	…
bn170826819	3.6	6.2	100	2.5	10.1	7.7	…	…	X	…	…
bn170906030	11.2	4.2	100	34.1	43.0	22.3	…	…	X	…	…
bn170921168	7.0	3.3	100	2.0	19.6	1.9	…	…	△	…	O
bn171010792	67.2	20.1	97	27.6	83.2	60.0	…	…	X	…	…
bn171102107	3.2	4.3	74	0.4	8.5	5.7	△	…	X	X	…
bn171119992	4.9	8.9	75	2.3	3.0	1.0	△	…	X	X	…
bn171210493	8.2	3.6	100	6.7	47.4	0.0	…	…	…	…	O
bn171227000	30.5	35.6	100	20.1	26.5	12.0	…	…	X	…	…

Note.
[a] The details of the criteria are in Section 2. The yellow and red flags are marked as triangle and an X, respectively.
(This table is available in machine-readable form.)

Appendix B
Spectral Analysis Result

In this section, we present the spectral analysis results of 32 pulses in 32 GRBs (see Sections 3 and 4 for details). For each GRB, we make a figure with six panels (see Figure 5 and figure set). The color gradient used in all panels indicates the elapsed time within the time interval shaded in pink in the top left panel, and later-time data are shown with a more saturated color. The top left panel shows the light curves in three energy

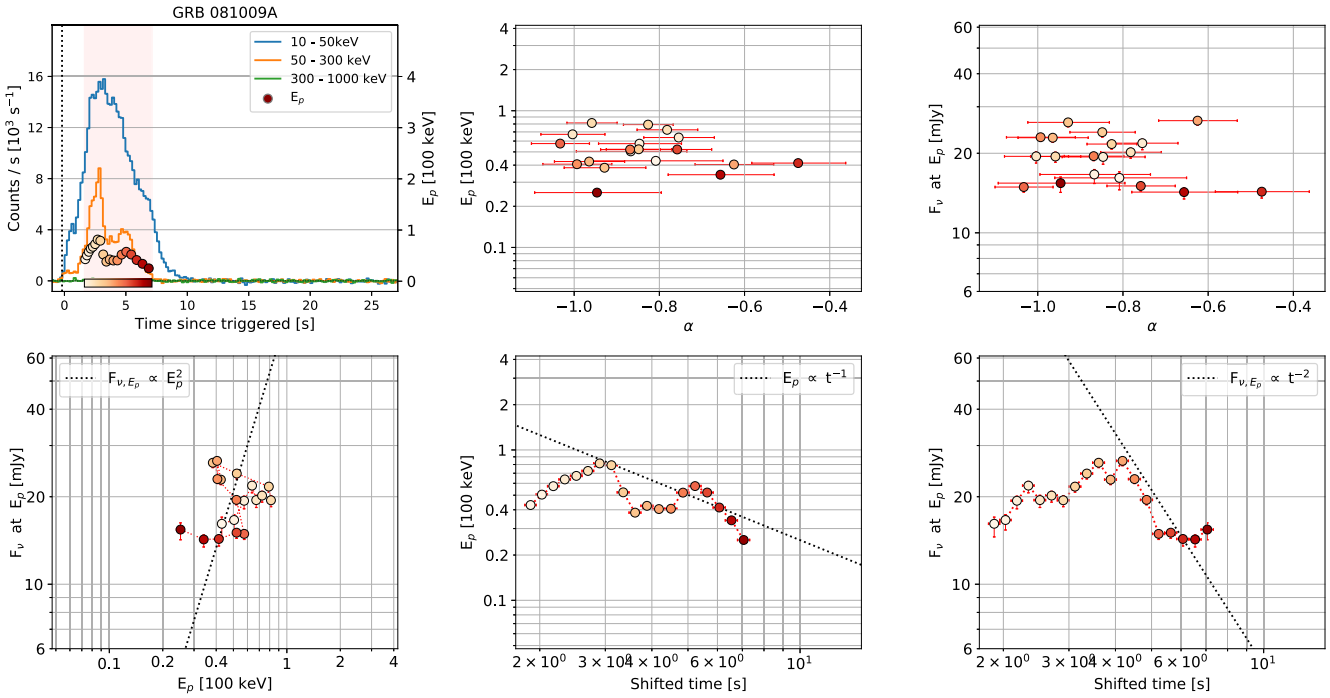

Figure 5. The color gradient used in all panels indicates the elapsed time within the time interval shaded in pink in the top left panel, and later-time data are shown with a more saturated color. The top left panel shows the light curves in three energy bands, with the temporal evolution of the $E_{\rm peak}$ points shaded with the gradient. The top middle and right panels show α vs. E_p and α vs. F_{ν,E_p}, respectively. The three bottom panels are intended to test the HLE expectation with three different perspectives, $F_{\nu,E_p} \propto E_p^2$, $E_p \propto t^{-1}$, and $F_{\nu,E_p} \propto t^{-2}$ from left to right.

(The complete figure set (32 images) is available.)

bands, with the temporal evolution of the $E_{\rm peak}$ points shaded with the gradient. The top middle and right panels show α versus E_p and α versus F_{ν,E_p}, respectively. The three bottom panels are intended to test the HLE expectation with three different perspectives, $F_{\nu,E_p} \propto E_p^2$, $E_p \propto t^{-1}$, and $F_{\nu,E_p} \propto t^{-2}$ from left to right.

ORCID iDs

Donggeun Tak https://orcid.org/0000-0002-9852-2469
Judith Racusin https://orcid.org/0000-0002-4744-9898
Bing Zhang https://orcid.org/0000-0002-9725-2524
Sylvain Guiriec https://orcid.org/0000-0001-5780-8770
Daniel Kocevski https://orcid.org/0000-0001-9201-4706
Bin-Bin Zhang https://orcid.org/0000-0003-4111-5958

References

Abdo, A. A., Ackermann, M., Ajello, M., et al. 2009, ApJL, 706, L138
Ackermann, M., Ajello, M., Asano, K., et al. 2011, ApJ, 729, 114
Ackermann, M., Asano, K., Atwood, W. B., et al. 2010, ApJ, 716, 1178
Ajello, M., Arimoto, M., Asano, K., et al. 2019, ApJL, 886, L33
Ascenzi, S., Oganesyan, G., Salafia, O. S., et al. 2020, A&A, 641, A61
Band, D., Matteson, J., Ford, L., et al. 1993, ApJ, 413, 281
Borgonovo, L., & Ryde, F. 2001, ApJ, 548, 770
Dermer, C. D. 2004, ApJ, 614, 284
Fenimore, E. E., Madras, C. D., & Nayakshin, S. 1996, ApJ, 473, 998
Ford, L. A., Band, D. L., Matteson, J. L., et al. 1995, ApJ, 439, 307
Genet, F., & Granot, J. 2009, MNRAS, 399, 1328
Golenetskii, S. V., Mazets, E. P., Aptekar, R. L., & Ilinskii, V. N. 1983, Natur, 306, 451
Granot, J., & Sari, R. 2002, ApJ, 568, 820
Gruber, D., Goldstein, A., Weller von Ahlefeld, V., et al. 2014, ApJS, 211, 12
Guiriec, S., Connaughton, V., Briggs, M. S., et al. 2011, ApJL, 727, L33
Guiriec, S., Kouveliotou, C., Daigne, F., et al. 2015, ApJ, 807, 148
Hakkila, J., & Preece, R. D. 2011, ApJ, 740, 104
Jia, L.-W., Uhm, Z. L., & Zhang, B. 2016, ApJS, 225, 17
Kargatis, V. E., Liang, E. P. & BATSE Team 1995, Ap&SS, 231, 177
Kocevski, D., Ryde, F., & Liang, E. 2003, ApJ, 596, 389
Kumar, P., & Panaitescu, A. 2000, ApJL, 541, L51
Kumar, P., & Zhang, B. 2015, PhR, 561, 1
Li, L., & Zhang, B. 2021, ApJS, 253, 43
Liang, E., & Kargatis, V. 1996, Natur, 381, 49
Liang, E. W., Zhang, B., O'Brien, P. T., et al. 2006, ApJ, 646, 351
Lu, R.-J., Liang, Y.-F., Lin, D.-B., et al. 2018, ApJ, 865, 153
Lu, R.-J., Wei, J.-J., Liang, E.-W., et al. 2012, ApJ, 756, 112
Narayana Bhat, P., Meegan, C. A., von Kienlin, A., et al. 2016, ApJS, 223, 28
Norris, J. P., Nemiroff, R. J., Bonnell, J. T., et al. 1996, ApJ, 459, 393
Nousek, J. A., Kouveliotou, C., Grupe, D., et al. 2006, ApJ, 642, 389
Oganesyan, G. 2020, in Proc. of the Yamada Conf. LXXI: Gamma-ray Bursts in the Gravitational Wave Era 2019, ed. T. Sakamoto, M. Serino, & S. Sugita (Yokohama: Yamada), 204, http://yokohamagrb2019.wikidot.com/proceedings
Ryde, F., & Svensson, R. 2002, ApJ, 566, 210
Sari, R., Piran, T., & Halpern, J. P. 1999, ApJL, 519, L17
Sari, R., Piran, T., & Narayan, R. 1998, ApJL, 497, L17
Scargle, J. D., Norris, J. P., Jackson, B., & Chiang, J. 2013, ApJ, 764, 167
Shen, R.-F., Song, L.-M., & Li, Z. 2005, MNRAS, 362, 59
Shenoy, A., Sonbas, E., Dermer, C., et al. 2013, ApJ, 778, 3
Tak, D., Guiriec, S., Uhm, Z. L., et al. 2019, ApJ, 876, 76
Uhm, S. L., Tak, D., Zhang, B., et al. 2022, ApJL, submitted (arXiv:2212.07094)
Uhm, Z. L., & Zhang, B. 2015, ApJ, 808, 33
Uhm, Z. L., & Zhang, B. 2016a, ApJL, 824, L16
Uhm, Z. L., & Zhang, B. 2016b, ApJ, 825, 97
Uhm, Z. L., Zhang, B., & Racusin, J. 2018, ApJ, 869, 100
von Kienlin, A., Meegan, C. A., Paciesas, W. S., et al. 2014, ApJS, 211, 13
Wang, J., Cen, X., Qian, T., Xu, J., & Wang, C. 2000, ApJ, 532, 267
Yamazaki, R., Toma, K., Ioka, K., & Nakamura, T. 2006, MNRAS, 369, 311
Yu, H.-F., Preece, R. D., Greiner, J., et al. 2016, A&A, 588, A135
Zhang, B., Fan, Y. Z., Dyks, J., et al. 2006, ApJ, 642, 354
Zhang, B., & Yan, H. 2011, ApJ, 726, 90
Zhang, B.-B., Liang, E.-W., & Zhang, B. 2007, ApJ, 666, 1002
Zhang, B.-B., Zhang, B., Liang, E.-W., & Wang, X.-Y. 2009, ApJL, 690, L10
Zhang, B.-B., Zhang, B., Liang, E.-W., et al. 2011, ApJ, 730, 141